Journal of Molecular Catalysis A: Chemical 349 (2011) 80–85

Contents lists available at SciVerse ScienceDirect

Journal of Molecular Catalysis A: Chemical

journal homepage: www.elsevier.com/locate/molcata

Nanocrystalline $ZnSb_2O_6$: Hydrothermal synthesis, electronic structure and photocatalytic activity

Wenjun Liu, Pingyong Lin, Hua Jin, Hun Xue, Yongfan Zhang, Zhaohui Li*

Research Institute of Photocatalysis, Fuzhou University, State Key Laboratory Breeding Base of Photocatalysis, Fuzhou 350002, PR China

ARTICLE INFO

Article history:
Received 29 June 2011
Received in revised form 25 August 2011
Accepted 27 August 2011
Available online 3 September 2011

Keywords:
Antimonate
Hydrothermal
Photocatalysis
Electronic structure
Density functional theory

ABSTRACT

Nanocrystalline $ZnSb_2O_6$ with small particles size and large BET specific area (131.4 m^2/g) was successfully prepared via a facile hydrothermal method directly from Sb_2O_5 and was fully characterized by X-ray diffraction (XRD), N_2-sorption BET surface area, UV–vis diffuse reflectance spectroscopy (DRS), scanning electron microscopy (SEM), transmission electron microscopy (TEM), and high-resolution transmission electron microscopy (HRTEM). The as-prepared $ZnSb_2O_6$ showed photocatalytic activity for the degradation of typical dyes rhodamine B (RhB) and methyl orange (MO) in the aqueous solution under UV irradiations. The electronic structure of $ZnSb_2O_6$ was studied by density functional theory (DFT). The different photocatalytic performance between $ZnSb_2O_6$ and $Sr_2Sb_2O_7$, another ternary antimonate photocatalyst, can be explained in terms of their different electronic structures and different crystal structures.

1. Introduction

Semiconductor-based photocatalytic oxidation has been established to be one of the most promising technologies for the environment remediation and has been employed in the treatment of all kinds of organic contaminants [1–3]. The effective application of photocatalysis in environmental remediation requires that the photocatalysts should have high photocatalytic efficiency. Therefore, during the past decade, a tremendous effort has been devoted to the development of new photocatalysts [4–11]. In addition to metal and non-metal ions doped TiO_2, single-phase-oxide-based photocatalysts consist of both d^0 and d^{10} central cations as well as a series of sulfides have been developed so far. However, some photocatalysts lack the long-term stability, while some show low activity, or require rigorous synthetic condition. The development of a new photocatalyst with high performance is still a great challenge in photocatalysis so far.

Recently, we and others have found that some metal oxides consist of central ion of Sb^{5+}, like $M_2Sb_2O_7$ (M = Sr^{2+} and Ca^{2+}) [12,13], $PbSb_2O_6$ [14], $BiSbO_4$ [15,16] and MSb_2O_6 (M = Ca, Sr and Ba) [17] showed photocatalytic activity for the degradation of benzene and organic dyes. All these antimonate-based photocatalysts contain distorted Sb–O polyhedra in their structure and imply that distorted Sb–O polyhedra may be the photocatalytic active. It would be interesting to explore the photocatalytic performance of other ternary antimonates with distorted Sb–O polyhedra and to elucidate the influence of the incorporated second metal ions on their photocatalytic activity.

$ZnSb_2O_6$ is another ternary antimonate which crystallizes in a tetragonal structure. The structure of $ZnSb_2O_6$ is built up from two edge-sharing SbO_6 octahedra (along *c* axis), sharing their corners with two other SbO_6 octahedra. Zn atoms are placed in the interstitials of SbO_6 octahedra. SbO_6 octahedra in $ZnSb_2O_6$ are distorted with three different Sb–O bonds (1.995, 1.998 and 2.011 Å). The existence of distorted SbO_6 octahedra in $ZnSb_2O_6$ stimulates us to study its photocatalytic performance. However, the only reported synthetic method for $ZnSb_2O_6$ is the solid state reaction method. It is generally known that products obtained via the solid state process are not favorable for the photocatalytic reaction since they usually contain undesirable phase and are usually inhomogeneous due to the high temperature sintering process. Soft chemical methods, such as hydrothermal/solvothermal method have been demonstrated to be effective methods in the preparation of nanocrystalline metal oxides with large specific surface area. Our previous study has found that nanocrystalline $Sr_2Sb_2O_7$ prepared from Sb_2O_5 via a hydrothermal method possesses high specific area and shows higher photocatalytic activity as compared to $Sr_2Sb_2O_7$ prepared via a traditional solid state reaction [13]. It would be interesting to see whether such a facile hydrothermal method can also be applied to the preparation of other nanocrystalline ternary antimonates, such as $ZnSb_2O_6$.

In this manuscript, we reported the synthesis of nanocrystalline $ZnSb_2O_6$ with small particle size and large BET specific surface area from Sb_2O_5 via a facile hydrothermal method. The photocatalytic

* Corresponding author. Fax: +86 591 83779105.
E-mail address: zhaohuili1969@yahoo.com (Z. Li).

1381-1169/$ – see front matter © 2011 Elsevier B.V. All rights reserved.
doi:10.1016/j.molcata.2011.08.023

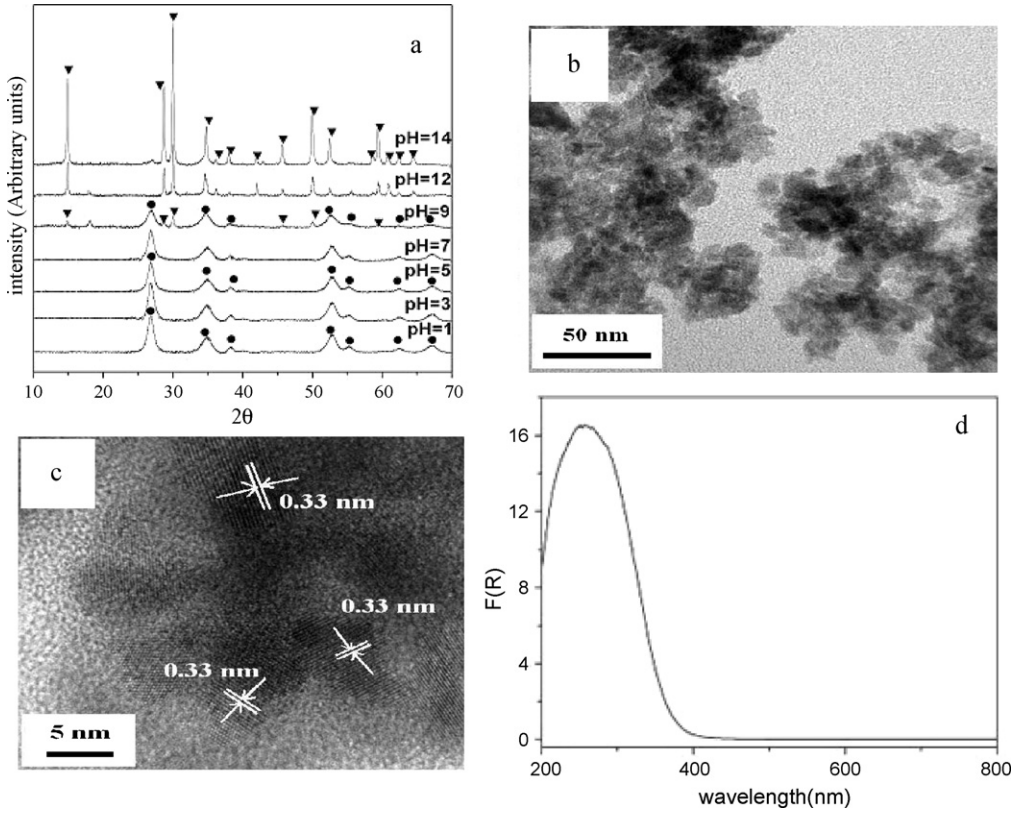

Fig. 1. (a) XRD patterns of the samples prepared at 180 °C for 48 h with different pHs. (●) $ZnSb_2O_6$; (▼) Sb_6O_{13}; (b) and (c) TEM and HRTEM images of $ZnSb_2O_6$ prepared at pH 1; (d) UV-DRS of $ZnSb_2O_6$ prepared at pH 1.

activity for the degradation of typical dyes such as rhodamine B (RhB) and methyl orange (MO) over the as-prepared nanocrystalline $ZnSb_2O_6$ was for the first time revealed. The electronic structure of $ZnSb_2O_6$ was studied by the density functional theory (DFT). Although the as-prepared $ZnSb_2O_6$ shows a larger specific surface area, its photocatalytic activity is lower as compared to another ternary antimonate photocatalyst $Sr_2Sb_2O_7$. The different photocatalytic performance between $ZnSb_2O_6$ and $Sr_2Sb_2O_7$ can be explained in terms of their different electronic structures and their different crystal structures.

2. Experimental

2.1. Syntheses

All of the reagents were of analytical grade and used without further purification. Nanocrystalline $ZnSb_2O_6$ samples were prepared by a hydrothermal method using $Zn(CH_3COO)_2{\cdot}2H_2O$ and Sb_2O_5 as starting materials. In a typical procedure, Sb_2O_5 powder (0.9705 g, 3.0 mmol) was added to 8 mL aqueous solution containing $Zn(CH_3COO)_2{\cdot}2H_2O$ (0.6585 g, 3.0 mmol) under vigorous stirring. The pH of the resulting mixture was adjusted by nitric acid solution or sodium hydrate solution under vigorous stirring. The mixture was loaded into a 23 mL Teflon-lined autoclave, filled with de-ionized water up to 70% of the total volume and sealed tightly. The autoclaves were kept at 180 °C for 48 h. After cooling to room temperature, the precipitate was collected, washed with distilled water and absolute ethanol for several times, and then dried in air at 80 °C.

2.2. Characterizations

X-ray diffraction (XRD) patterns were collected on a Bruker D8 Advance X-ray diffractometer with CuK_α radiation. The accelerating voltage and the applied current were 40 kV and 40 mA, respectively. Data were recorded at a scanning rate of 0.004° 2θ s^{-1} in the 2θ range of 10–70°. It was used to identify the phase present and their crystallite size. The crystallite size was calculated from X-ray line broadening analysis by Scherer equation: $D = 0.89\lambda/\beta\cos\theta$, where D is the crystal size in nm, λ is the CuK_α wavelength (0.15406 nm), β is the half-width of the peak in rad, and θ is the corresponding diffraction angle. The specific surface area of the samples was measured by nitrogen sorption at 77 K on ASAP 2020 instrument and calculated by the BET method. UV–visible absorption spectra (UV-DRS) of the powders were obtained for the dry-pressed disk samples using a UV–visible spectrophotometer (Cary 500 Scan Spectrophotometers, Varian, USA). $BaSO_4$ was used as a reflectance standard in the UV–visible diffuse reflectance experiment. The transmission electron microscopy (TEM) and high resolution transmission electron microscopy (HRTEM) images were measured by JEOL model JEM 2010 EX instrument at the accelerating voltage of 200 kV. The powder particles were supported on a carbon film coated on a 3 mm diameter fine-mesh copper grid. A suspension of the sample in ethanol was sonicated and a drop was dripped on the support film. Morphology of the sample was characterized by field emission scanning electron microscopy (SEM) (JSM-6700F).

2.3. Photocatalytic activity measurements

The photocatalytic activity of the as-prepared nanocrystalline $ZnSb_2O_6$ was evaluated by the degradation typical dyes RhB and MO in an aqueous solution under UV irradiations. Four 4-W UV lamps with a wavelength centered at 254 nm (Philips, TUV 4W/G4 T5) were used as illuminating source. Aqueous photocatalytic reactions were performed in a quartz tube with 4.6 cm inner diameter and 17 cm length. 150 mg of $ZnSb_2O_6$ was added into 150 mL of RhB

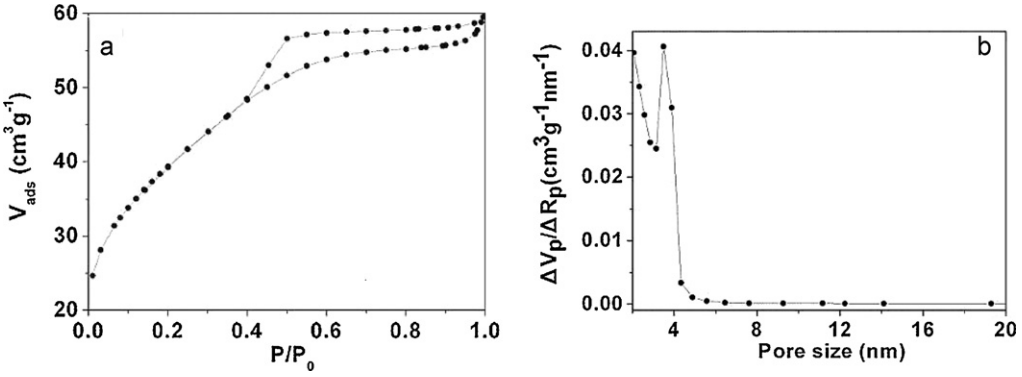

Fig. 2. (a) Nitrogen adsorption–desorption isotherm and (b) pore size distribution plot for $ZnSb_2O_6$ prepared at pH 1.

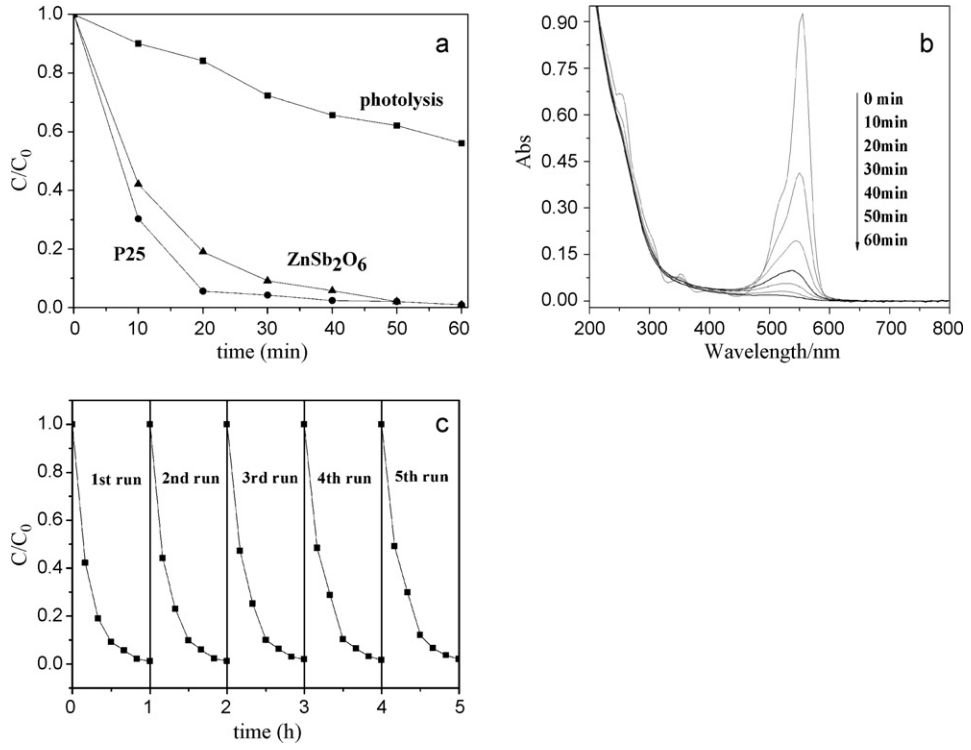

Fig. 3. (a) Temporal changes of RhB concentration as monitored by the UV–vis absorption spectra at 554 nm over illuminated $ZnSb_2O_6$, illuminated P25 and UV irradiations only; (b) temporal absorption spectral patterns of RhB during the photodegradation process over the as-prepared $ZnSb_2O_6$; (c) cycling runs in the photocatalytic degradation of RhB over illuminated $ZnSb_2O_6$.

solution (10^{-5} mol/L) and stirred overnight before irradiation to ensure that adsorption/desorption equilibrium had been reached. At given irradiation time intervals, 4 mL of the suspensions were collected, centrifuged, and filtered through a Millipore filter to separate the photocatalyst particles. The degraded solutions of RhB and MO were analyzed by a Varian Cary 500 Scan UV–vis spectrophotometer. The absorption peak at 554 nm for RhB was monitored. The percentage of degradation is reported as C/C_0. C is the absorption of RhB at each irradiated time interval of the maximum peak of the absorption spectrum at wavelength 554 nm. C_0 is the absorption of the starting concentration when adsorption/desorption equilibrium was achieved. The measurement of the photocatalytic activity of $ZnSb_2O_6$ for the degradation of MO is similar to that of RhB except that the initial concentration of MO is 20 ppm. The absorption peak at 464 nm for MO was monitored.

2.4. Theoretical calculations

The structural optimizations of $ZnSb_2O_6$ and $Sr_2Sb_2O_7$ were performed by using the projector-augmented wave (PAW) formalism of DFT, as implemented in the Vienna ab initio simulations package (VASP) [18–21], and the Perdew–Burke–Ernzerhof (PBE) type exchange-correlation was adopted [22]. In the calculations, the cell shape and the atomic positions were allowed to be relaxed at an energy cutoff of 400 eV and a $5 \times 5 \times 5$ Monkhorst–Pack k-point grid.

3. Results and discussion

The XRD patterns of the resultant products through the hydrothermal process at 180 °C for 48 h under different pH value

are shown in Fig. 1a. It is observed that the pH value plays an important role in controlling the composition of the final products. For pH value in the region of 1–7, pure $ZnSb_2O_6$ (JCPDS 751037) can be obtained. When pH value is 9, the resultant product is a mixture of $ZnSb_2O_6$ and Sb_6O_{13}. When pH value is higher than 12, only Sb_6O_{13} can be obtained. This indicates that pure $ZnSb_2O_6$ can only be obtained under acidic condition. The XRD pattern of the as-prepared $ZnSb_2O_6$ sample shows that the peaks are wide, indicating that the average crystallite sizes of the $ZnSb_2O_6$ samples are small. The average crystallite sizes calculated from the Scherrer equation are about 6 nm for $ZnSb_2O_6$ sample prepared when pH value is 1.

Unlike $Sr_2Sb_2O_7$, which are obtained under strong basic condition, pure $ZnSb_2O_6$ can only be obtained under acidic condition. The unable to obtain $ZnSb_2O_6$ under strong basic condition can be well explained by the amphoteric nature of the zinc ion. It is generally known that under high pH value, Zn ion exists as $Zn(OH)_4^{2-}$ and the dominant species of Sb(V) exists as $Sb(OH)_6^-$. It would be difficult for the anionic $Zn(OH)_4^{2-}$ to react with the anionic $Sb(OH)_6^-$ to give $ZnSb_2O_6$ nanoparticles. On the contrary, under acidic condition, Sb_2O_5 exists mainly as $(HSb_2O_6)^-$ [23], which can react with Zn^{2+} to give $ZnSb_2O_6$ nanoparticles. The chemical reactions involved can be formulated as follows:

$$Sb_2O_5 + H_2O \rightarrow [HSb_2O_6]^- + H^+$$

$$[HSb_2O_6]^- + Zn^{2+} \rightarrow ZnSb_2O_6 + H^+$$

The typical TEM image of $ZnSb_2O_6$ prepared at pH value of 1 is shown in Fig. 1b. The as-prepared $ZnSb_2O_6$ consists entirely of small particles with average size at around 6 nm, which is consistent with the result obtained from Scherrer formula. The HRTEM image shows clear lattice fringes (Fig. 1c). The fringes of $d = 0.33$ nm matches that of the (2 2 0) plane of $ZnSb_2O_6$. The EDS indicates the presence of Zn, Sb and O. The atomic ratio of Zn and Sb is about stoichiometry 1:2 and indicates that no impurity exists. The UV-DRS spectra of $ZnSb_2O_7$ show that the absorption edge locates at ca. 370 nm, corresponding to a band gap of about 3.3 eV (Fig. 1d). The N_2-sorption isotherm for the as-prepared $ZnSb_2O_6$ exhibits stepwise adsorption and desorption (type IV isotherm), indicative of a mesoporous solid. The average pore size for the as-prepared $ZnSb_2O_6$ is 4.0 nm with a narrow distribution of pore size (Fig. 2). This porosity is originated from the inter-particle porosity as evidenced in the TEM image. The BET specific surface area for the as-prepared $ZnSb_2O_6$ is determined to be 131.4 m^2/g. Therefore the hydrothermal method is a practical method in the preparation of nanocrystalline $ZnSb_2O_6$ with small particles and large BET specific surface.

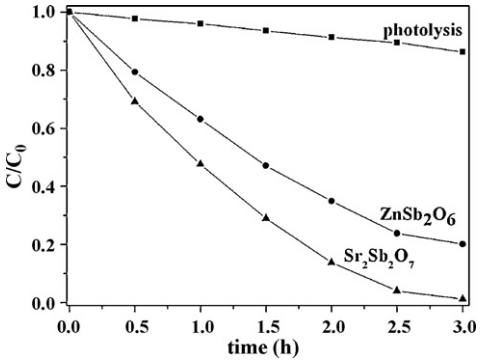

Fig. 4. Temporal changes of MO concentration as monitored by the UV–vis absorption spectra at 464 nm on the as-prepared $ZnSb_2O_6$ and $Sr_2Sb_2O_7$.

The photocatalytic activity of the as-prepared $ZnSb_2O_6$ was evaluated by the degradation of typical dyes RhB and MO under UV light irradiations. Temporal changes in the concentration of RhB as monitored by the maximal absorption in UV–vis spectra at 554 nm over $ZnSb_2O_6$ are shown in Fig. 3a. After having irradiated for about 40 min, about 95% of RhB was degraded and a complete degradation of RhB occurred in 60 min. On the contrary, only about 40% of RhB was degraded with pure UV irradiations. This indicates that $ZnSb_2O_6$ can degrade RhB effectively. The photocatalytic activity of the as-prepared nanocrystalline $ZnSb_2O_6$ is comparable to the commercial Degussa P25 (Fig. 3a). The temporal evolutions of the spectral changes taking place during the photodegradation of RhB over $ZnSb_2O_6$ are shown in Fig. 3b. The shift of the main absorbance of RhB (at 554 nm) to a shorter wavelength during the irradiations is negligible. This indicates a rather facile cleavage of the whole conjugated chromophore structure instead of the de-ethylation of RhB occurs [24]. Besides this, the as-prepared nanocrystalline $ZnSb_2O_6$ shows high stability during the photocatalytic reaction and there is no obvious loss of photocatalytic activity after five runs (Fig. 3c). $ZnSb_2O_6$ also shows photocatalytic activity for the degradation for MO, another typical dye (Fig. 4).

Although $ZnSb_2O_6$ shows photocatalytic activity for the degradation of dyes, its photocatalytic activity is lower as compared to $Sr_2Sb_2O_7$, another ternary p-block semiconductor photocatalyst. As shown in Fig. 4, an almost complete degradation of MO was observed over illuminated $Sr_2Sb_2O_7$ in 3 h, while only about 78% of

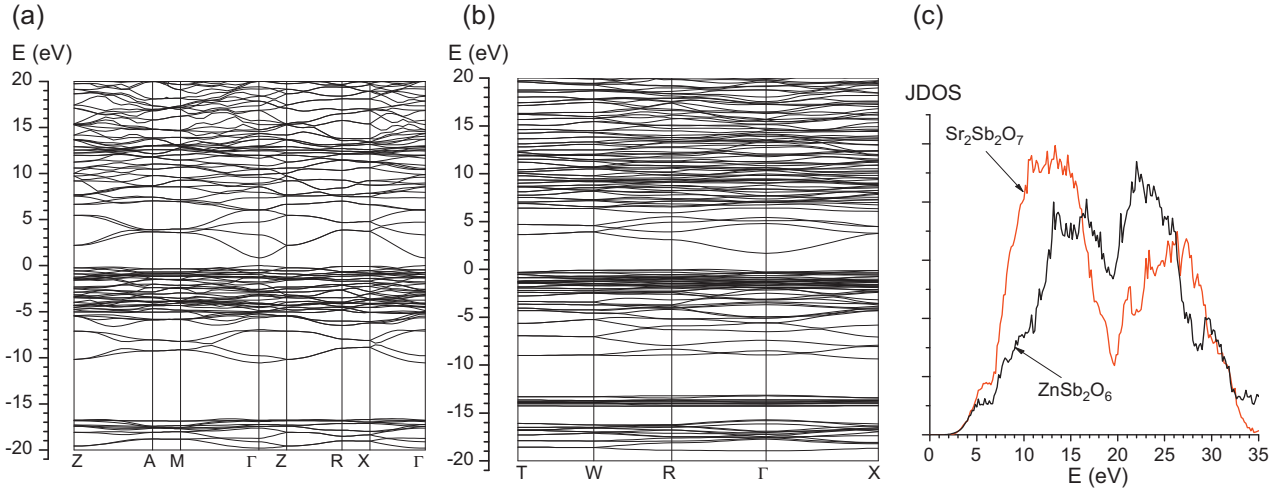

Fig. 5. Band structures of (a) $ZnSb_2O_6$ and (b) $Sr_2Sb_2O_7$, and (c) the joint DOSs (JDOS) of two compounds. In figures (a) and (b), the valence-band maximum is taken as the energy zero.

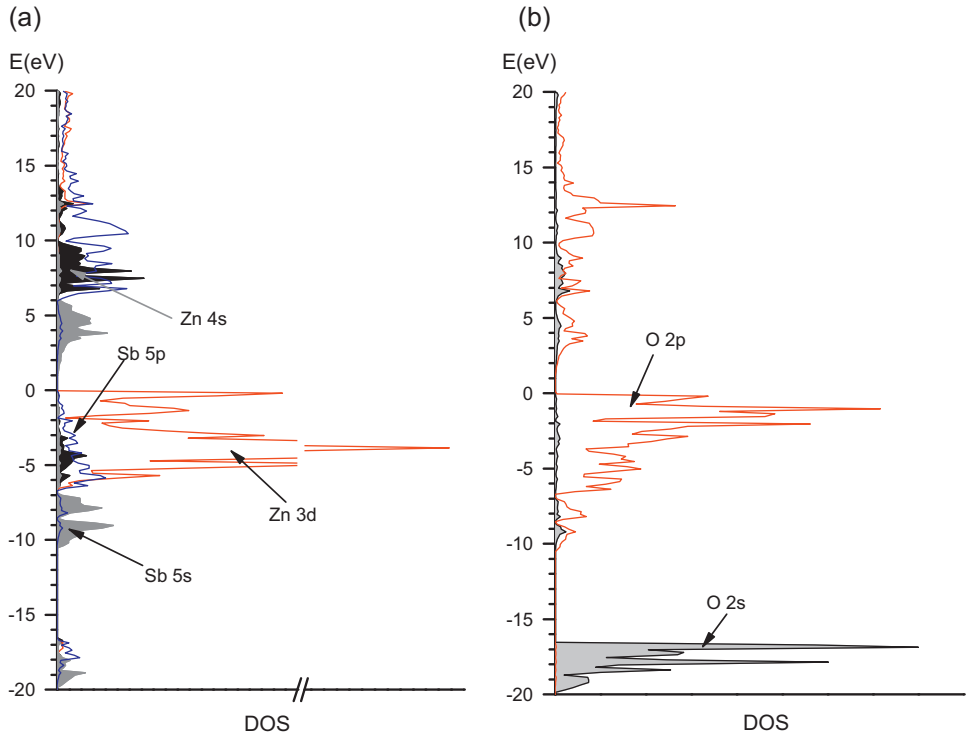

Fig. 6. (a) Partial DOSs of Zn and Sb atoms; (b) partial DOSs of O 2s and 2p states of $ZnSb_2O_6$. In the figures, the valence-band maximum is taken as the energy zero.

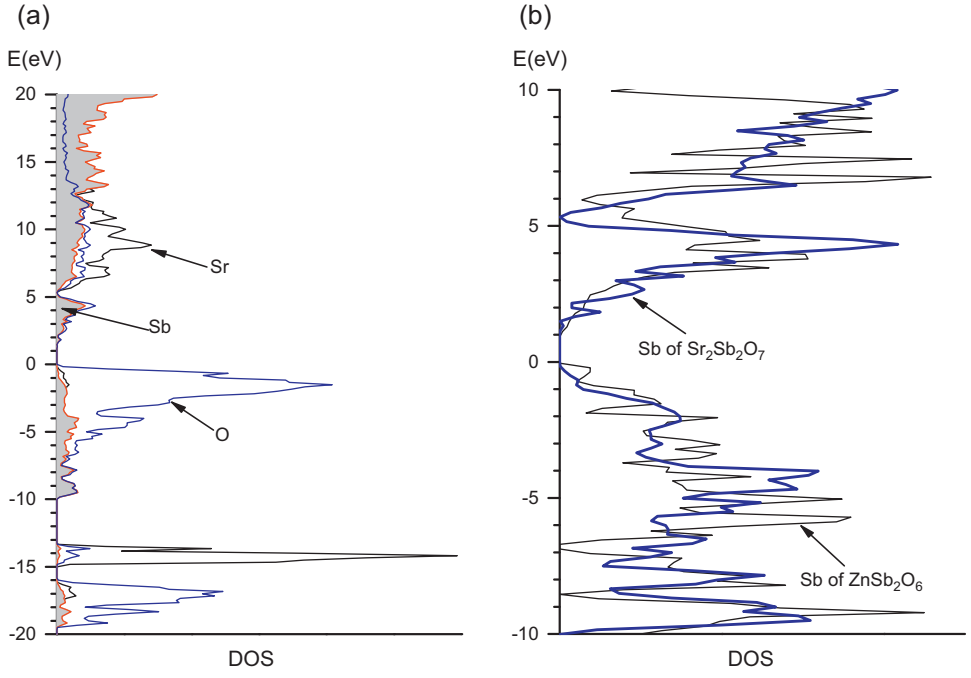

Fig. 7. (a) Partial DOSs of Sr, Sb and O atoms of $Sr_2Sb_2O_7$; (b) comparison of Sb states of two compounds. In the figures, the valence-band maximum is taken as the energy zero.

MO was degraded over $ZnSb_2O_6$ under similar condition. Considering the much larger specific surface area of $ZnSb_2O_6$ (131.4 m^2/g) as compared to $Sr_2Sb_2O_7$ (24.8 m^2/g), this result is little surprising. The larger band gap of $Sr_2Sb_2O_7$ (4.2 eV) compared to $ZnSb_2O_6$ (3.3 eV) may contribute to its higher photocatalytic activity, but may not be the sole factor. It is generally believed that both the electronic structure and the crystal structure of a semiconductor may influence its photocatalytic activity. Therefore, the electronic structure of $ZnSb_2O_6$ was calculated by the DFT and compared to that of $Sr_2Sb_2O_7$.

The band structures of $ZnSb_2O_6$ and $Sr_2Sb_2O_7$ are shown in Fig. 5a and b, respectively. A direct band gap of 0.84 eV is found at Γ point for $ZnSb_2O_6$, while a larger band gap (1.70 eV) is obtained for $Sr_2Sb_2O_7$. Although the predicted band gap difference between these two semiconductors (0.86 eV) is consistent with the experimental value (0.9 eV), the calculated band gaps of both $ZnSb_2O_6$ and

$Sr_2Sb_2O_7$ are smaller than the values of 3.3 eV and 4.2 eV obtained by UV–vis DRS. The underestimate of the band gap for semiconductors or insulators calculated by the DFT method is due to the insufficient cancellation of the self-interaction correction inherent in the local exchange functional [25,26].

For $ZnSb_2O_6$, based on the partial density of states (DOSs) displayed in Fig. 6, the energy bands in the range between −20 and −17 eV are mainly derived from O 2s states, and the σ-bonding interactions between Sb 5s and O 2p orbitals give rise to the energy bands appeared in the region from −10 eV to −7 eV. The components of VB are somewhat complicated, in which Zn 4s/3d, Sb 5p and O 2p states are found. However, in the top of VB, Zn 3d and O 2p are the dominant components. For the CB, it is mainly associated with the σ*-antibonding interactions between Sb 5s and O 2p states.

For $Sr_2Sb_2O_7$, besides the value of the band gap, additional differences in the electronic structures are observed with respect to $ZnSb_2O_6$. The top of VB is dominated by O 2p states, and the contribution from cation (Sr^{2+}) atoms is small (Fig. 7a). The comparison of the distributions from Sb states in $ZnSb_2O_6$ and $Sr_2Sb_2O_7$ reveals that there are more Sb states in the region near the bottom of CB for $Sr_2Sb_2O_7$ (Fig. 7b). In addition to this, the joint DOSs of $ZnSb_2O_6$ and $Sr_2Sb_2O_7$ have also been calculated to study the possibility of the excitation of the valence electrons (Fig. 5c). It can be clearly seen that more electrons are excited in $Sr_2Sb_2O_7$ when the energy of the absorbed photon is smaller than 17 eV. All these make $Sr_2Sb_2O_7$ a more efficient photocatalyst as compared to $ZnSb_2O_6$. The theoretical results indicate that the change of the second metal significantly affects both the components and the position of CB and VB in these ternary antimonates.

Besides their different electronic structures, the different crystal structures of $ZnSb_2O_6$ and $Sr_2Sb_2O_7$ may also contribute to their different photocatalytic performance. Recently Huang and co-workers reported that there exists a correlation between the packing factor (PF) and photocatalytic activity based on a survey of a series of inorganic oxides consisting of d^{10} and d^0 cations [17,27]. A calculation reveals a PF value of 66.08% for $ZnSb_2O_6$ and 64.36% for $Sr_2Sb_2O_7$. We believe that the lower PF of $Sr_2Sb_2O_7$ may also contribute to its higher photocatalytic activity since a lower PF is correlated with a higher electron–hole separation and transportation, and would result in better photocatalytic activity.

4. Conclusion

In summary, nanocrystalline $ZnSb_2O_6$ has been successfully prepared by a facile hydrothermal method. The as-prepared $ZnSb_2O_6$ can effectively degrade typical dyes such as MO and RhB. The different photocatalytic performance between $ZnSb_2O_6$ and $Sr_2Sb_2O_7$ can be explained in terms of their different electronic structures and different crystal structures. DFT calculations indicate that the incorporation of different second metal in these ternary antimonates may change their electronic structures and affect their photocatalytic activity. The preparations of other ternary antimonates and the investigations of their photocatalytic activity are still going on in our laboratory.

Acknowledgements

This work was supported by National Natural Science Foundation of China (20977016, 90922022) and Program for Changjiang Scholars and Innovative Research Team in University (PCSIRT0818). This work is also supported by fund of Fujian Provincial Key Laboratory of Nanomaterials (NM10-01). The NSF of Fujian province for Distinguished Young Investigator Grant (2009J06004) for Z. Li is also acknowledged.

References

[1] M.R. Hoffmann, S.T. Martin, W. Choi, D.W. Bahnemann, Chem. Rev. 95 (1995) 69–96.
[2] A. Fujishima, T.N. Rao, D.A. Tryk, J. Photochem. Photobiol. C 1 (2000) 1–21.
[3] C.C. Chen, W.H. Ma, J.C. Zhao, Chem. Soc. Rev. 39 (2010) 4206–4219.
[4] S.X. Ouyang, J.H. Ye, J. Am. Chem. Soc. 133 (2011) 7757–7763.
[5] Z.H. Ai, L.Z. Zhang, S.C. Lee, J. Phys. Chem. C 114 (2010) 18594–18600.
[6] J.G. Yu, G.P. Dai, B.B. Huang, J. Phys. Chem. C 113 (2009) 16394–16401.
[7] H.F. Shi, Z.S. Li, J.H. Kou, J.H. Ye, Z.G. Zou, J. Phys. Chem. C 115 (2011) 145–157.
[8] S. Zhu, T. Xu, H. Fu, J. Zhao, Y. Zhu, Environ. Sci. Technol. 41 (2007) 6234–6239.
[9] Y. Bi, S. Ouyang, J. Cao, J. Ye, Phys. Chem. Chem. Phys. 13 (2011) 10071.
[10] H. Dong, Z. Li, X. Xu, Z. Ding, L. Wu, X. Wang, X. Fu, Appl. Catal. B: Environ. 89 (2009) 551–556.
[11] Y. Chen, S. Hu, W. Liu, X. Chen, L. Wu, X. Wang, P. Liu, Z. Li, Dalton Trans. 40 (2011) 2607–2613.
[12] X.P. Lin, F.Q. Huang, W.D. Wang, Y.M. Wang, Y.J. Xia, J.L. Shi, Appl. Catal. A: Gen. 313 (2006) 213–218.
[13] H. Xue, Z.H. Li, L. Wu, Z.X. Ding, X.X. Wang, X.Z. Fu, J. Phys. Chem. C 112 (2008) 5850–5855.
[14] K.L. Zhang, X.P. Lin, F.Q. Huang, Y.M. Wang, J. Mol. Catal. A: Chem. 258 (2006) 185–190.
[15] X.P. Lin, F.Q. Huang, W.D. Wang, K.L. Zhang, Appl. Catal. A: Gen. 307 (2006) 257–262.
[16] Q.Q. You, Y.H. Fu, Z.X. Ding, L. Wu, X. Wang, Z.H. Li, Dalton Trans. 40 (2011) 5774–5780.
[17] X. Lin, J. Wu, X. Lv, Z. Shan, W. Wang, F. Huang, Phys. Chem. Chem. Phys. 11 (2009) 10047–10052.
[18] G. Kresse, J. Hafner, Phys. Rev. B 47 (1993) 558–561.
[19] G. Kresse, J. Hafner, Phys. Rev. B 49 (1994) 14251–14269.
[20] G. Kresse, J. Furthmuller, Phys. Rev. B 54 (1996) 11169–11186.
[21] G. Kresse, J. Furthmuller, Comput. Mater. Sci. 6 (1996) 15–50.
[22] J.P. Perdew, K. Burke, M. Ernzerhof, Phys. Rev. Lett. 77 (1996) 3865–3868.
[23] S.H. Gate, E. Richardson, J. Inorg. Nucl. Chem. 23 (1961) 257–263.
[24] C.C. Chen, W. Zhao, J.C. Zhao, Chem. Eur. J. 10 (2004) 1956–1965.
[25] J.P. Perdew, M. Levy, Phys. Rev. Lett. 51 (1983) 1884–1887.
[26] A. Zunger, J.P. Perdew, G.L. Oliver, Solid State Commun. 34 (1980) 933–936.
[27] J. Wu, F. Huang, Z. Shan, Y. Wang, Dalton Trans. 40 (2011) 6906–6911.